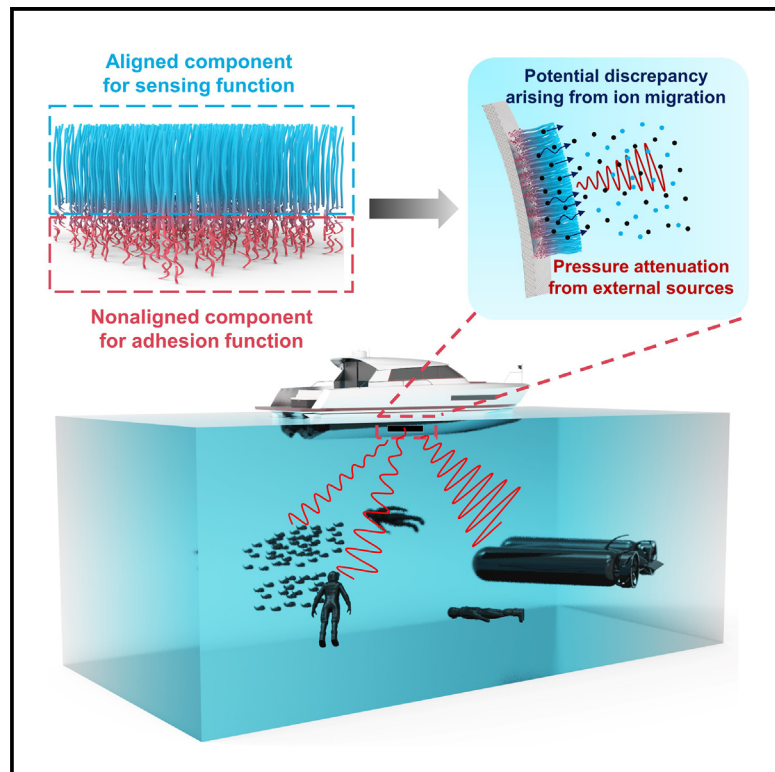


Underwater target detection using hybrid carbon nanotube self-adhesive sensors

Graphical abstract



Authors

Huajian Li, Yifan Liu, Zonglin Ye,
Qifan Zhang, Shaolong Yang, Ming Xu

Correspondence

ming.xu@hust.edu.cn

In brief

An underwater non-contact target detection sensor is created using a self-adhesive hybrid structured carbon nanotube assembly. This sensor can detect subtle underwater pressure stimuli down to 18 mPa, aided by its self-adhesion property to reduce interference and provide stable fixation to the carrier, such as the hull of a ship. Recognition of underwater targets is demonstrated by using artificial neural networks to interpret the signal produced by the sensor. The sensing system offers a solution for long-range passive target detection and location tracking in underwater environments.

Highlights

- The sensor is composed of aligned and nonaligned carbon nanotubes
- The hybrid structure adhesion provides the ability to detect underwater pressure waves
- The tested detection limit for pressure waves in sea water is 18 mPa
- An artificial neural network can help distinguish signals from different targets



Explore

Early prototypes with exciting performance
and new methodology

Li et al., 2024, Device 2, 100223
January 19, 2024 © 2023 The Author(s).
Published by Elsevier Inc.
<https://doi.org/10.1016/j.device.2023.100223>

Article

Underwater target detection using hybrid carbon nanotube self-adhesive sensors

Huajian Li,^{1,2} Yifan Liu,³ Zonglin Ye,¹ Qifan Zhang,¹ Shaolong Yang,³ and Ming Xu^{1,2,4,*}

¹School of Materials Science and Engineering, State Key Laboratory of Material Processing and Die and Mould Technology, Huazhong University of Science and Technology, Wuhan 430074, China

²Shenzhen Huazhong University of Science and Technology Research Institute, Shenzhen, Guangdong, China

³School of Naval Architecture and Ocean Engineering, Huazhong University of Science and Technology, Wuhan 430074, China

⁴Lead contact

*Correspondence: ming.xu@hust.edu.cn

<https://doi.org/10.1016/j.device.2023.100223>

THE BIGGER PICTURE In the underwater domain, the ability to passively detect and identify submerged targets without the use of a probing acoustic pulse is essential for monitoring marine ecosystems, resources, and infrastructure. However, the underwater environment poses challenges, including limited visibility, dynamic water conditions, and the demand for rugged and dependable sensing technologies. To address these challenges, we designed a self-adhesive pressure sensor for the passive detection of underwater targets through the use of a hybrid structure of aligned and nonaligned carbon nanotubes. Bolstered by artificial neural networks, the sensing system can detect different targets based on their different frequencies, and it has the potential to deconvolute signals from multiple targets by using a setup of multiple sensors.

SUMMARY

The passive detection of underwater targets relies on sensitive pressure sensors. In this study, we introduce a self-adhesive pressure sensor for non-contact underwater target detection. The sensors are made of a hybrid carbon nanotube assembly. The aligned component fosters dense contacts between the nanotubes, which are responsible for the sensor's ability to detect pressure changes as small as 18 mPa, with 99.82% linearity in the 18–178 mPa range, and a lifespan exceeding 10,000 cycles. The nonaligned component ensures robust underwater adhesion while minimizing impedance and self-noise and enhancing target tracking. By using artificial neural networks to analyze the signal, the sensor demonstrates its ability to identify targets with different frequencies. In field trials, the sensor achieved the detection of a 1.25-m target boat motivated by a three-bladed propeller with the characteristic noise frequency of 3 Hz while moving at a speed between 2.7 and 3.5 knots.

INTRODUCTION

Object detection is a crucial function in many underwater applications, ranging from scientific research (e.g., marine biology and environmental monitoring), industry (e.g., underwater surveillance of mining and oil extraction operations), and military (e.g., threat detection).^{1,2} For example, by utilizing underwater target recognition and monitoring the signals emitted by marine species within specific waters, one can categorize populations and identify non-native species for studying the balance of regional ecosystems. Underwater target detection and tracking can also help improve underwater communication and navigation systems for manned and unmanned submarines. However, challenges such as medium attenuation, signal interference, and variable water conditions must be addressed to ensure the effectiveness of non-contact underwater detection.^{3–5}

The operational modes of underwater sensors can be divided into active detection (i.e., sending out soundwaves and listening for the echoes) and passive detection (i.e., listening for sounds made by the targets). While active detection possesses the advantages of high-resolution imaging, low noise interference, and the ability to modulate the frequency of the emitted acoustic signal for different target ranges, the method requires a high-power signal transmission source to transmit signals, which increases the burden on the power system. Active detection systems are also easily detectable and traceable by potential adversaries because of the soundwaves they send out.^{6–8} Passive detection offers a stealthy alternative, with low power consumption, and the potential to cover a larger range without being limited by the emission distance, making it a promising solution for detecting targets over extensive areas.^{9–15} Without the use of a probing pulse, passive detection systems are limited only by

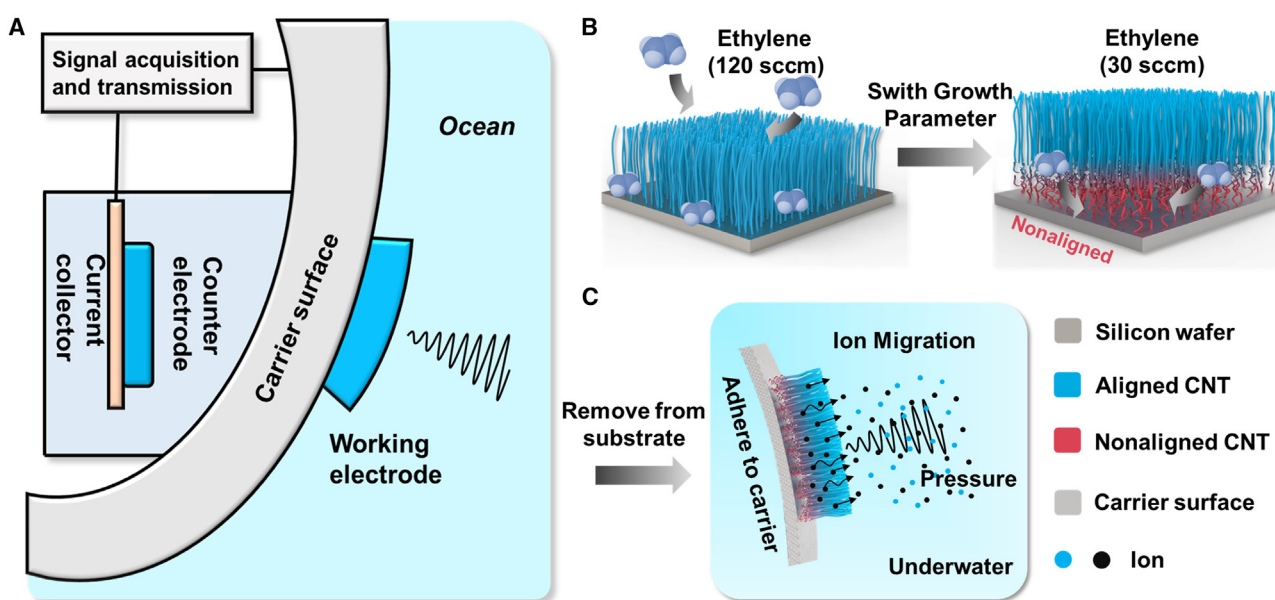


Figure 1. Application scenario and fabrication of the self-adhesive pressure sensor

(A) Structure of the self-adhesive pressure sensor.

(B) Fabrication process of hybrid CNT assembly.

(C) Working mechanism of our self-adhesive underwater pressure sensor.

the sensitivity and resolution of the sensors.^{16–20} Recent advancements have made progress in pressure detection, reaching as low as 0.59 Pa through contact-based modes utilizing hydrophobic ionic gels.²¹ Nevertheless, the achievement of non-contact pressure sensing in an underwater environment remains relatively scarce.

In this work, we present an innovative self-adhesive underwater pressure sensor with the capacity of non-contact pressures detection based on a special hybrid carbon nanotube (CNT) assembly that comprises aligned and nonaligned components within a single structure. The aligned component, characterized by densified intertube contact, allows for exceptional pressure sensitivity, detecting pressures as low as 18 mPa while maintaining a linearity of 99.82% across its detection range. Furthermore, the nonaligned component exhibits a shear adhesion strength of 23.24 N/cm², enabling the 5 × 5 mm sensor to withstand water sprays of 1.67 L/s (or 1.67 kg/s) and underwater travel at 10 km/h. By harnessing the sensitivity and pressure detection capabilities, combined with the computational power of artificial neural networks, the sensor demonstrates effective signal analysis and classification for various underwater targets. These advancements in the self-adhesive underwater pressure sensor open up new possibilities for non-contact pressure detection and underwater target recognition.

RESULTS AND DISCUSSIONS

Fabrication and characterization of self-adhesive underwater pressure sensor

Figure 1A depicts the device setup of the self-adhesive pressure sensing system. The sensor primarily comprises of a working

electrode affixed to the outer surface of the carrier for measuring the underwater pressure. A counter electrode is positioned inside the carrier with a current collector to gather the charge signals.

A hybrid architecture is implemented in the synthesis of the CNT array using the two-stage water-assisted chemical vapor deposition (CVD) shown in Figure 1B.²² Silicon wafers were used as the substrate, onto which a Fe catalyst (3 nm) and Al₂O₃ buffer layer (40 nm) are deposited by physical vacuum deposition. Afterward, the catalyst-coated substrate was heated up to 780°C in a controlled hydrogen atmosphere (300 standard cubic centimeters per minute [sccm], 400 s). During this process, the surface-diffusing Fe atoms agglomerated on catalyst particles, initiating CNT growth. In the initial growth stage, a supply of ethylene (120 sccm) is subjected to catalytic decomposition, resulting in the formation of a highly oriented CNT array with a density of 32.65 mg/cm³ and an average length of 790 μm. In the second stage, the ethylene is reduced to (30 sccm), causing only a fraction of the catalysts to contribute to CNT growth. As a result, the density and crowding effect of the CNT array decrease, leading to a shift to a nonaligned structure with a density of 14.39 mg/cm³ and an average length of 205 μm.^{23,24} It is worth noting that, when synthesized separately, the aligned and nonaligned CNTs are structurally different compared with those grown using the two-step method.²² The CNT assembly grown using the two-step method possesses similar microstructures across the aligned and nonaligned CNTs, including their average wall number (between 2 and 3), high purity (~99.7%), and crystallinity (I_G/I_D of 1.21) (Figures S1–S3). It is important to note that our hybrid CNT assembly do not denote the amalgamation of two distinct

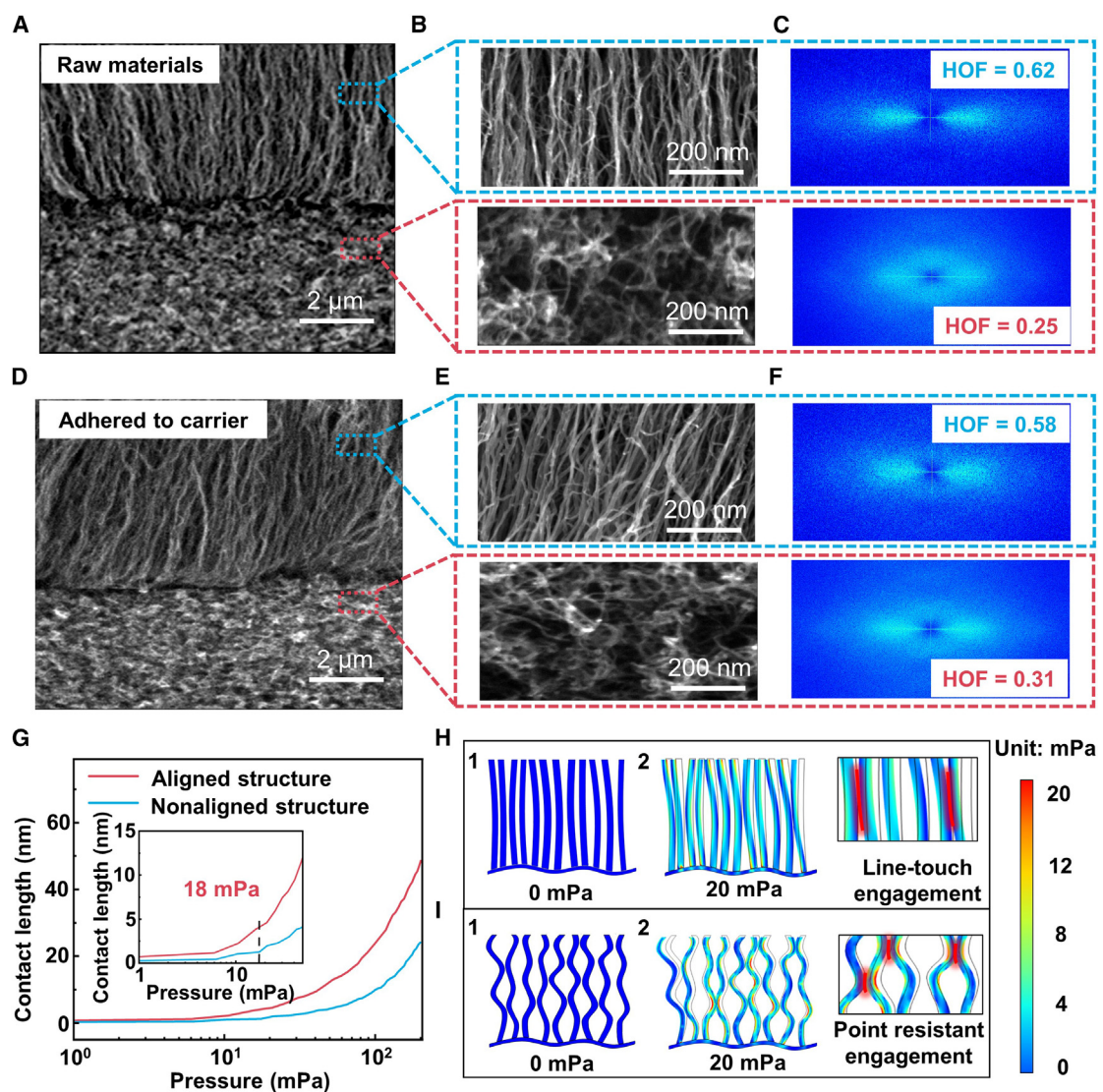


Figure 2. Working mechanism of self-adhesive sensing

(A and B) SEM images of the hybrid CNT assembly before adhesion.

(C) Fourier fast transform (FFT) images of the aligned and nonaligned components of the hybrid CNT assembly before adhesion.

(D and E) SEM images of the hybrid CNT assembly adhered to the carrier.

(F) FFT images of the aligned and nonaligned components of the hybrid CNT assembly adhered to the carrier.

(G) Intertube contact length vs. pressure of the aligned structure and nonaligned structure.

(H) Structural evolution of the aligned CNTs upon pressure increase to 20 mPa; the contact length increased with pressure increase.

(I) Structural evolution of the nonaligned CNTs upon pressure increase to 20 mPa; it was difficult to increase the contact length due to the bending structure.

structural compositions; rather, they encompass an integral connection between the nonaligned component and the aligned component within a unified structure. Therefore, the hybrid CNT assembly exhibits ample mechanical strength for complete detachment from the silicon substrate. Subsequently, it adheres to the carrier surface through its inherent adhesion properties under pre-pressure (Figure 1C). We have achieved large-area growth of raw materials (shown in Figure S4), whose size and shape can be further modified using techniques such as laser cutting. The performance stability within the same batch of our materials is approximately 93%.

Scanning electron microscopy (SEM) analysis presents a closer look at the hybrid CNT structure. It showcases an interface within the assembly due to the disparity in density between the aligned and nonaligned components. The upper portion of the structure exhibits characteristics akin to the aligned CNT component, while the lower portion mirrors the attributes of the nonaligned CNT component (Figures 2A and 2B). This stands in contrast to independent aligned and nonaligned CNT assemblies, which exhibit a homogeneous structure (Figures S5A and S5C). To quantitatively evaluate the hybrid structure, we employed the calculation of Herman's orientation factor (HOF)

and generated Fourier fast transform images based on the SEM images (Figures 2C, S5B, and S5D).²³ The results indicate that the aligned component of the hybrid CNT assembly demonstrates a comparable HOF value of 0.62, akin to the aligned CNT array with an HOF of 0.67. Similarly, the nonaligned component located at the bottom of the hybrid CNT assembly exhibits HOF values of 0.25, closely aligning with the HOF of the nonaligned CNTs (0.35). The density and orientation disparity between the aligned and nonaligned components within the hybrid CNT assembly lead to a distinct inflection point on the stress-strain curve at approximately ~16% strain (Figure S6). This inflection point signifies that the nonaligned component of the hybrid CNT assembly undergoes complete compression and flattening, reaching its maximum deformation under the applied strain. In contrast, the aligned portion remains protected and unaffected by the strain. Furthermore, the stress-strain curve illustrates that the nonaligned CNT component exhibits a lower elastic modulus when compared with their arrayed counterparts. This lower modulus implies a heightened susceptibility to deformation under preloading conditions, leading to a more pronounced conformity to the substrate and the establishment of robust adhesion.

Working mechanism of the CNT assembly for self-adhesion and pressure sensing

When submerged in a saline solution such as seawater, the CNTs were fully infiltrated by electrolytes, providing the largest electrochemically accessible surface area. Upon the application of pressure exerted by underwater targets, the CNTs experienced tilting or bending, resulting in intertube contact. This caused a reduction in the electrochemically accessible surface area, leading to ion migration. Consequently, a potential discrepancy was generated, giving rise to an open-circuit voltage (OCV) in response to the pressure exerted by underwater targets (Figure 1C).² The density of aligned components, crucial for establishing extensive tube contacts, amplifies ion migration and elevates sensitivity. Meanwhile, the nonaligned component provides self-adhesion capabilities, which removes the need for external fixation methods, such as adhesive tapes, minimizing potential interference, and enhancing the stability of the sensor.

Guided by the stress-strain curve, an appropriate force (~0.04 MPa corresponding to the inflection point) was applied to the hybrid CNT assembly to help it adhere to the carrier (Figures 2D and 2E). It can be observed that the aligned component maintains its original structure, while the nonaligned component was compressed to get into contact with the carrier. The HOF calculation shows that the aligned component experiences a slight decrease in HOF from 0.62 to 0.58 as a result of preloading. Conversely, the nonaligned component exhibits an increase in HOF from 0.25 to 0.31 due to structural flattening perpendicular to the direction of pressure (Figure 2F). The uniform construction of both the aligned and nonaligned CNTs leads to consistent deformation across their structures (Figure S7), although the adhering process results in an inevitable loss of orientation in the aligned array.

We employed COMSOL Multiphysics software to analyze the changes in CNT interaction within the sensing component as a response to applied pressure (Figure S8). In accordance with

the SEM observation (Figures 2D and 2E), the aligned CNTs in the simulation function as the sensing component, and have a slightly wavy structure due to the pre-loading. Figure 2G illustrates the comparison of intertube contacts under the increment of pressure from 0 to 200 mPa. The contact length was measured directly from the COMSOL simulation results from Figure S9. The aligned assembly demonstrates a larger increase in contact length compared with the nonaligned assembly. Upon closer examination of the ultralow pressure stage (Figure 2G, inset), the aligned structure exhibits detectable intertube contacts from 1 to ~20 mPa, resulting from an increased number of migrating ions and a greater potential signal. In contrast, the nonaligned structure shows much less variations in intertube contacts.

Figures 2H, 2I, and S9 offer visual insights into the structural variations within the intertube configuration when subjected to ultralow pressure conditions from 0 to 20 mPa. In ultralow pressure settings, aligned CNTs exhibit a distinct structural reaction by forming interconnected "line-touch" contacts (Video S1). Picture this as CNTs aligning side by side and connecting along linear paths, forming a network of intertube contacts. As the pressure mounts, this alignment leads to an abundance of these linear contacts (Figure 2H). The densely arranged structure that results from this line-touch contact is instrumental for our sensor's performance. As more CNTs come into direct contact and line up together, the transmission of forces and the migration of ions are more efficient. This efficiency in ion migration and force transmission ultimately leads to the generation of detectable signals to even the minutest changes in pressure. We termed this phenomenon the "line-touch engagement," which leads to a more compact and densely arranged structure and enhances its sensitivity to pressure changes. In contrast, the nonaligned structure displays a different form of intertube interactions, which we termed "point resistant engagement," and include the buckling, kinking, and bending of the CNTs in different directions (Video S1). The random nature of these contact points contributes to a distributed load-bearing capacity and higher deformation tolerance compared with the aligned CNTs, which resist intertube engagement under ultralow pressure (Figure 2I). Because of the irregular buckling and bending of the nonaligned CNTs, there are variations in contact length observed within the pressure range of less than 20 mPa, indicating a barrier to ultralow pressure detection of nonaligned structure. It can be inferred that preserving the aligned structure during the adhesion process to the carrier is crucial for maintaining the function of ultralow pressure detection.

Adhesion properties of the underwater self-adhesive pressure sensors

As discussed above, the structural advantage of the hybrid CNT assembly lies in its ability to preserve the aligned structure, which serves as the sensing component, through the achievement of self-adhesion functionality. The underwater adhesion properties of the pressure sensors were evaluated through the custom setup of adhesion measurement with the detailed illustrations in Figure S10. As the adhesion strength of CNTs to the substrate primarily stems from van der Waals forces and is

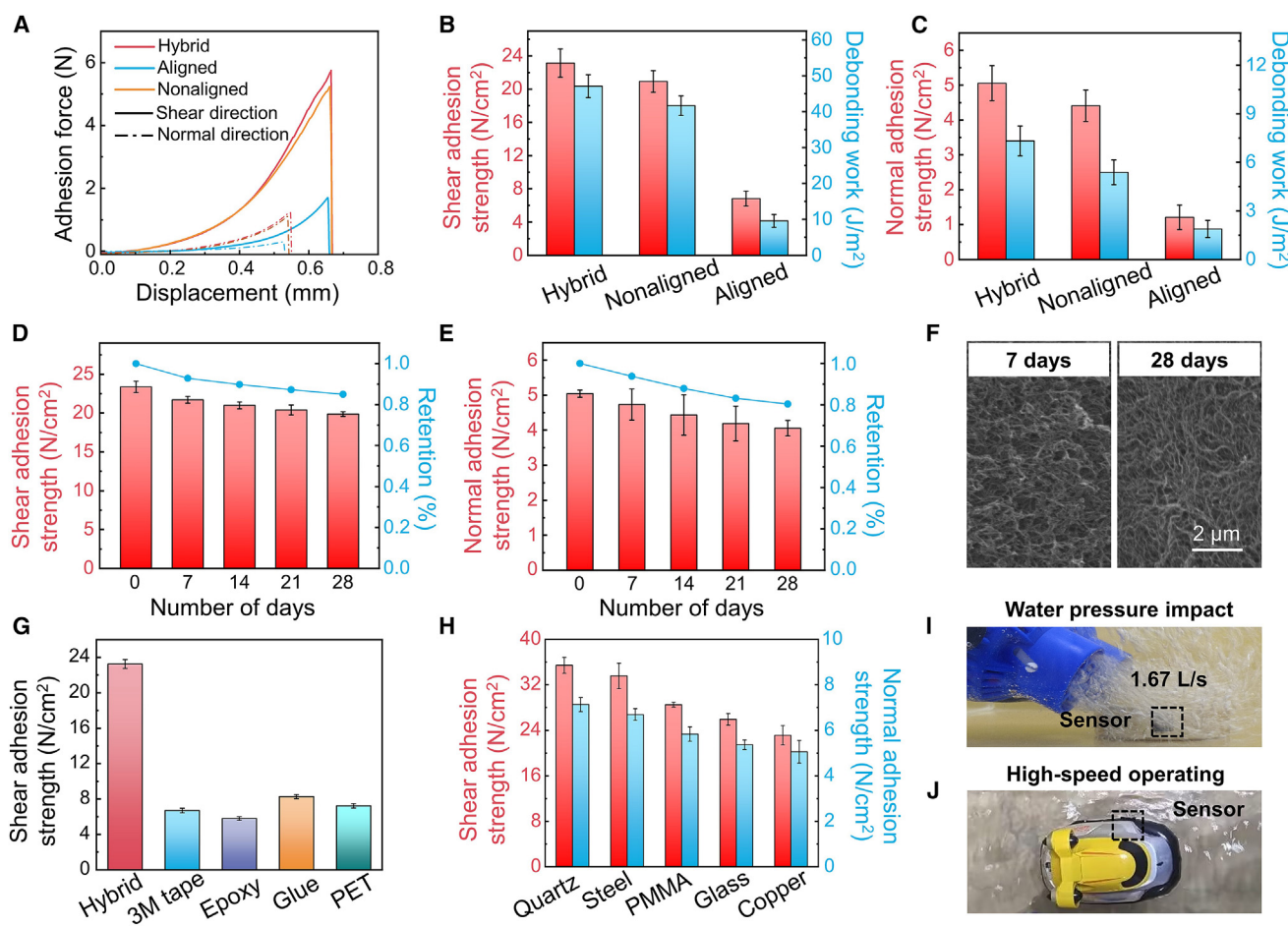


Figure 3. Adhesion performance of self-adhesive underwater pressure sensors

- (A) Shear and normal force vs. displacement curves of self-adhesive underwater pressure sensors based on hybrid CNT assembly, aligned CNT array, and nonaligned CNT assembly.
- (B) Shear adhesion performance of self-adhesive underwater pressure sensors based on hybrid CNT assembly, aligned CNT array, and nonaligned CNT assembly. Error bars, SD; n = 3.
- (C) Normal adhesion performance of self-adhesive underwater pressure sensors based on hybrid CNT assembly, aligned CNT array, and nonaligned CNT assembly. Error bars, SD; n = 3.
- (D) Long-lasting shear adhesion values of self-adhesive pressure sensor based on hybrid CNT assembly for different numbers of days. Error bars, SD; n = 3.
- (E) Long-lasting normal adhesion values of self-adhesive pressure sensor based on hybrid CNT assembly for different numbers of days. Error bars, SD; n = 3.
- (F) The SEM images of hybrid CNT assembly immersed in 0.6 mol/L NaCl solution after 7 and 28 days.
- (G) Shear adhesion performance of a self-adhesive pressure sensor based on hybrid CNT assembly compared with other materials in water tested on copper substrate. Error bars, SD; n = 3.
- (H) Shear and normal adhesion performance of self-adhesive pressure sensor based on hybrid CNT assembly to various substrates in water. Error bars, SD; n = 3.
- (I) Water pressure impact test.
- (J) Remote control boat operating test.

affected by the extent of contact realized through CNT assembly deformation during pre-loading conditions,²⁵ the selection of preloading force is important for ensuring adhesion. In a test using a copper substrate, the pre-loading forces for the aligned, hybrid, and nonaligned CNT assemblies are determined by their specific stress-strain curves in Figure S6. Their adhesion strength (i.e., adhesion force per unit area) and debonding work are read from the force-displacement curves in Figure 3A, which presents their debonding process from the copper substrate in the shear and normal directions. The hybrid CNT assembly exhibits the highest adhesion strength, measuring 23.24 ± 1.72 N/cm² for shear direction and 5.05 ± 0.51 N/cm² for normal direction. The nonaligned CNTs displays a comparable shear adhesion strength of 20.92 ± 1.31 N/cm² and normal adhesion strength of 4.41 ± 0.45 N/cm² with hybrid CNTs, and the aligned CNT array displays a shear adhesion force of 6.82 ± 0.92 N/cm² and normal adhesion force of 1.21 ± 0.35 N/cm², respectively (Figures 3B and 3C).

The enhancement in adhesion strength can be attributed to the formation of a random network structure from the preloading of hybrid CNTs and nonaligned CNTs. This structure facilitates increased contact area and provides additional opportunities

for interfacial interactions with the substrates. The expanded contact area allows for more efficient distribution of forces over a larger region, thereby reducing the probability of localized failure. Moreover, in comparison with aligned CNTs, the flexibility and conformability of hybrid CNTs and nonaligned CNTs enable improved contact with the surface irregularities of substrates further enhancing the adhesion performance. Therefore, greater debonding work is required to overcome the adhesion forces of hybrid ($47.11 \pm 3.21 \text{ J/m}^2$ for shear and $7.32 \pm 0.92 \text{ J/m}^2$ for normal) and nonaligned CNTs (with values of $41.67 \pm 2.73 \text{ J/m}^2$ for shear and $5.38 \pm 0.77 \text{ J/m}^2$ for normal). These values are roughly four to five times higher than those found in aligned CNTs ($9.56 \pm 1.88 \text{ J/m}^2$ for shear and $1.88 \pm 0.53 \text{ J/m}^2$ for normal).

To assess the long-term reliability of underwater operations, the time-dependent adhesion performance of the hybrid structure is presented in Figures 3D and 3E. After a 7-day immersion period, the shear and normal adhesion strengths of the hybrid CNT assemblies measure 21.71 ± 0.44 and $4.73 \pm 0.41 \text{ N/cm}^2$, respectively, exhibiting adhesion retention rates of 92.85% and 93.81%. After 28 days of immersion, the adhesion strength remains at 19.87 ± 0.31 and $4.05 \pm 0.22 \text{ N/cm}^2$, with retention rates of 85.02% and 80.35%, respectively. Figure 3F provides a comparison of the SEM images of the hybrid CNT assemblies peeled from the copper substrate after 7 and 28 days of immersion. The random attachment mode is retained, albeit with a slight increase in porosity due to water penetration. The chemical stability of the CNTs prevents the attachment of microorganisms even after 28 days of immersion in 0.6 mol/L NaCl solutions. In addition, no size variations are observed for the hybrid CNTs through optical investigations (Figure S11). These advantages contribute to the underwater adhesion performance of the hybrid CNTs, which shows the adhesive strength of 2–3 times higher than the commercially available adhesive materials we tested using the same conditions (Figure 3G).

Taking into account the diversity of carrier materials, the substrate adaptability is evaluated through the adhesion measurements of the pressure sensor based on hybrid CNTs on various substrates including quartz, steel, PMMA, glass, and copper (see Figure 3H). We provide roughness data for these substrates measured by AFM in Figure S12. Despite a reduction in adhesion strength as substrate roughness increases, our device demonstrates robust adhesion in both shear and normal directions. As demonstrated, these adhesion properties allow the structure to withstand water pressure impacts of up to 1.67 L/s generated by a water pump (Figure 3I). This characteristic ensures the reliable performance of our pressure sensor in turbulent conditions (Figure 3J).

We would like to stress that the adhesion process does not compromise the integral connection between the adhesive part (i.e., the nonaligned component) and the sensing part (i.e., the aligned component) within the device (Figures S13A and S13B). It highlights that all adhesion strengths result from nonaligned component detachment from various substrates, further affirming the superior resilience of the connection between aligned and nonaligned components over material-substrate adhesion (Figure S13C).

Sensing properties of the underwater self-adhesive pressure sensors

After securing the CNT working electrode onto a copper substrate and assembling the underwater pressure sensor, we evaluated its sensing performance through an experiment for non-contact mPa-pressure sensing. These tests encompassed a range from 18 to 178 mPa, as depicted in Figure S14. A comparative analysis of the response, in terms of the OCV, was conducted for the self-adhesive underwater pressure sensors based on hybrid CNT assembly, aligned CNT array, and nonaligned CNT assembly across a pressure range of 18 mPa (the instrument limitation) to 178 mPa (Figure 4A). The pressure sensor based on only aligned CNTs was adhered to the current collector using an acrylic double-sided tape (3M) due to unsatisfactory adhesion performance. In all, the pressure sensor utilizing the hybrid CNTs exhibited the lowest detectable limit of 18 mPa, which is consistent with the outcomes obtained from finite element simulation. In comparison, the pressure sensor utilizing aligned and nonaligned CNTs had detectable limits of 45 and 79 mPa, respectively.

The sensor based on hybrid CNTs also exhibited the highest sensitivity of 0.89 mV/Pa with the detection range from 18 to 178 mPa with a linearity of 99.82%. In comparison, the sensing performance of the sensor using aligned CNT array was affected by the tape, leading to a degraded sensitivity of 0.78 mV/Pa over the pressure range from 45 to 178 mPa with a linearity of 99.69%, and the nonaligned CNT-based sensor demonstrated the lowest sensitivity of 0.48 mV/Pa over the pressure range of 79–178 mPa with a linearity of 98.51%. The real-time OCV signals for the three structured working electrodes at 18 mPa are shown in Figure S15. It is evident that the sensor utilizing hybrid CNTs displayed an improved signal-to-noise ratio, attributed to its higher OCV signal in response to low pressure. In contrast, the pressure sensor utilizing aligned CNTs exhibited a considerably weaker OCV signal that closely approached the noise level, rendering it arduous to discern its distinctive characteristics. This phenomenon could likely be attributed to the presence of tape, which potentially introduces interface impedance and interferes with pressure absorption. The OCV of the nonaligned structure was heavily influenced by noise signals due to the similarities in amplitude. The lack of uniformity in intertube contacts leads to a less ordered and more heterogeneous response to applied pressure.

Figure 4B illustrates the real-time OCV signals of the self-adhesive pressure sensor based on the hybrid CNT assembly under varying magnitudes of sinusoidal pressure at a frequency of 5 Hz. As the applied pressure increased incrementally from 18 to 178 mPa, the OCV output correspondingly increased from 0.19 to 1.65 mV. Notably, the sensor operated in a self-powered manner without the need for an external power supply. When driven by a pressure of 178 mPa at a frequency of 5 Hz, the OCV of the hybrid-CNT-based sensor increased from 0.44 to 1.66 mV accompanied by the load resistance increased from 50 to 250 Ω . The peak power of $0.19 \mu\text{W}/\text{m}^2$ was obtained for a load resistance of 137 Ω based on the fitted curve (Figure S16). By eliminating the reliance on batteries, the sensors reduce the risk of power failure or depletion, ensuring continuous and reliable operation. This characteristic is especially important for

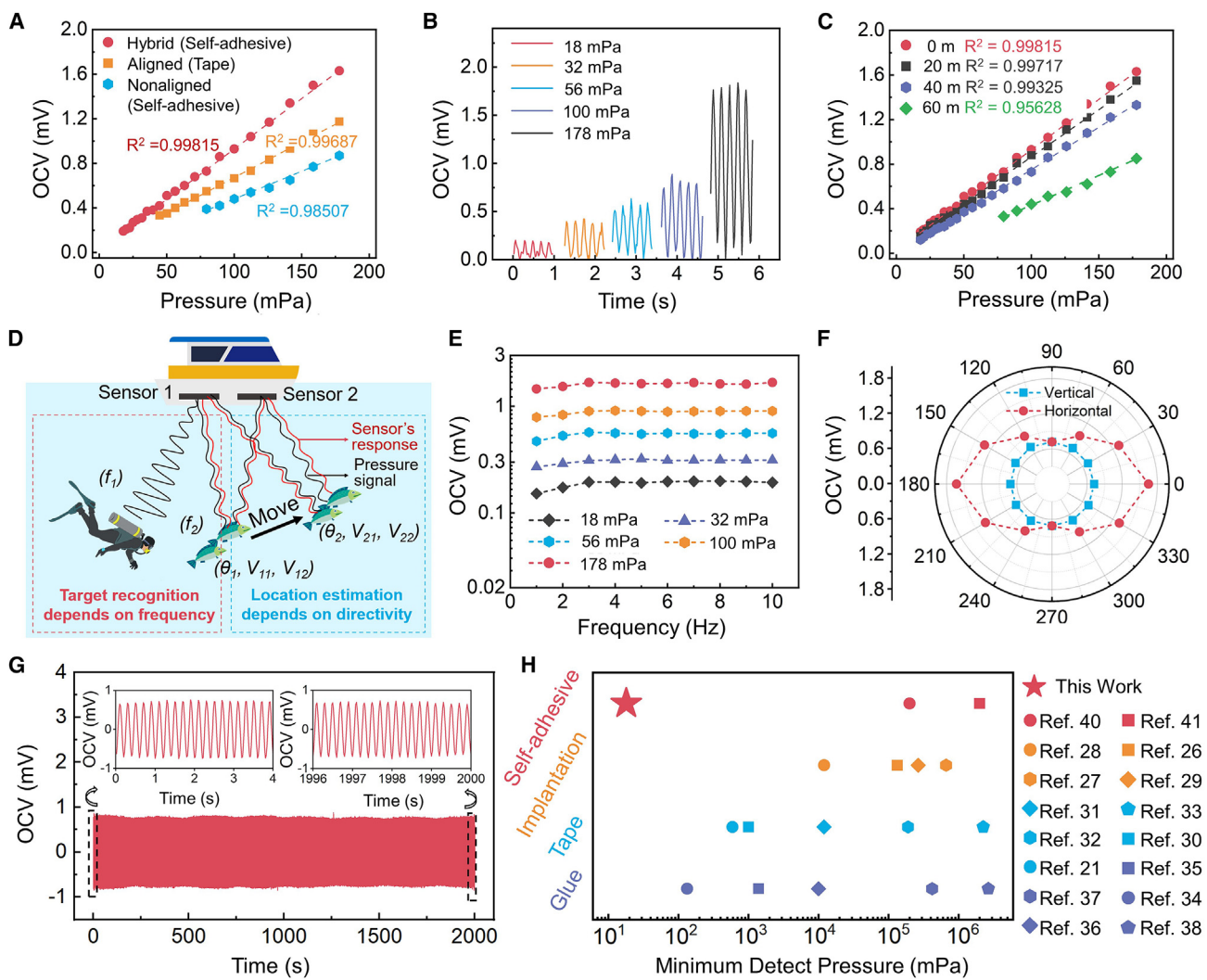


Figure 4. Sensing performance of self-adhesive underwater pressure sensors

- (A) Open-circuit voltage vs. sinusoidal pressure at 5 Hz of hybrid, aligned, and nonaligned structural self-adhesive pressure sensors.
- (B) Real-time open-circuit voltage of a hybrid structural self-adhesive pressure sensor at 5 Hz sinusoidal pressure with a range from 18 to 178 mPa.
- (C) Response of hybrid CNT-based sensor to varied pressures at depths of 0 m (0 kPa), 20 m (200 kPa), 40 m (400 kPa), and 60 m (600 kPa) under water (simulated).
- (D) Target recognition through frequency response and location estimation through sensor directivity.
- (E) Open-circuit voltage vs. frequency at sinusoidal pressure with a range from 18 to 178 mPa.
- (F) Directivity of hybrid structural self-adhesive pressure sensor at 5 Hz sinusoidal pressure.
- (G) Stability of hybrid structural self-adhesive pressure sensor at 5 Hz sinusoidal pressure. Inset: the first (left) and last (right) 20 cycles of 10,000 cycles.
- (H) Comparison with other pressure sensors with different integration methods.

long-term non-contact target detections where maintenance or sensor retrieval may not be feasible.

To investigate the capabilities of the hybrid CNT-based sensor in deep-sea environments, we replicated conditions akin to deep-sea testing by applying pre-pressure to the sensor while ensuring robust sample fixation through the use of a specialized fixture (Figure 4C). Considering the water pressure conversion rate of approximately 10 kPa/m of water depth, we applied pre-pressures of 0, 200, 400, and 600 kPa using a water tank and hydrostatic motor system to replicate conditions akin to water depths of 0, 20, 4, and 60 m, respectively. The pressure

detection capability of our sensor remains strong, with the same detection range of 18–178 mPa at 40 m under water, albeit with a slight reduction in linearity from 0.99815 (at 0 m) to 0.99325 (at 40 m) due to the minor deformation of the CNTs under pressure. At the 60 m depth, a more noticeable reduction in performance occurs due to extensive structural bending and compression of the aligned CNT component.

The sensor also exhibits frequency stability and vertical directivity. By analyzing the signal, it is possible to discern target categories based on distinct target frequencies (e.g., distinguishing between an aquanaut emitting frequency f_1 and a fish emitting

frequency f_2). Regarding the localization of underwater targets, this is achieved through the use of a sensor array. For instance, when encountering a fish at position θ_1 , the responses of sensor 1 and sensor 2 are denoted as V_{11} and V_{12} , respectively. Conversely, for a fish at position θ_2 , the corresponding responses for sensor 1 and sensor 2 are represented as V_{21} and V_{22} . This sensor array-based approach enables precise determination of the location of the underwater targets (Figure 4D). Figure 4E illustrates the output response of the sensor at various frequency within a pressure range from 18 to 178 mPa between 1 and 10 Hz. The frequency stability is rooted in its mode of operation. The CNT-based sensing material generates potential differences (SCC and OCV signals) when subjected to pressure-induced deformations through electrochemical processes and ionic migration on the CNT surfaces. When the CNT material is fully saturated, the migration rate of ions on the CNT surface far exceeds the rate of deformation itself. The dominance of ion migration, especially within the 1–10 Hz range, combined with the exceptional mechanical stability of the hybrid CNT assembly across the frequency range (Figure S17), assures minimal impact on the sensor frequency response within this frequency range. The results indicate that, across this frequency range, the output variations are 21.24%, 13.74%, 15.77%, 12.51%, and 12.93% corresponding to the applied pressures of 18, 32, 56, 100, and 178 mPa, respectively.

The directivity of the self-adhesive underwater pressure sensor is presented in Figure 4F. During the testing process, a pressure of 178 mPa at a frequency of 5 Hz was applied to the sensor, and the sensor was rotated around the speaker in 30° increments for testing, as shown in Figure S18. The results demonstrated that, in the horizontal direction, the output response remained stable at 0.71 mV, indicating consistent response regardless of direction. However, in the vertical direction, the device exhibited distinct directivity. When pressure was applied directly facing the sample at 0°, the sensor exhibited a maximum response of 1.65 mV. As the angle of applied pressure deviated, the response gradually decreased. At 90°, the sensing response matched the value obtained in the horizontal direction, which was 0.71 mV. With further angle increases, the response gradually increased again, reaching a maximum value of 1.65 mV at 180°. The output response of the sensor in the range of 180–360° mirrored the response obtained in the range of 0–180°. This behavior could be attributed to the directivity of the sensing component of hybrid CNT-based pressure sensors in the vertical direction.

The results of the cycle performance test, shown in Figure 4G, demonstrate that the sensor maintains a steady output response of 1.65 mV under cyclic pressure loading at a frequency of 5 Hz and a magnitude of 178 mPa over 10,000 cycles. The inset displays real-time response curves for the first and last 20 cycles, showing minimal change in the output response to pressure. Figure S19 presents the mechanical stability of the hybrid CNT assembly adhered to a steel substrate. Subjected to 200 mPa, almost no fluctuation was observed on the elastic modulus, the loss modulus, and damping ratio over 10,000 cycles. Furthermore, the sensor demonstrates a rapid response time of approximately 18 ms to pressure signals, enabling swift detection of underwater targets (Figure S20).

Compared with other pressure sensors with various integration methods reported such as implanted,^{26–29} tape based,^{21,30–33} and glue-fixed sensors,^{34–38} the self-adhesive approach holds the advantage of easy installation and low interface impedance. There have been cases that self-adhesive underwater pressure sensors based on hydrogel materials being proven instrumental in monitoring human activities underwater and exploring the marine environment.^{17,39} The sensor presented in this work achieve an extension of the minimum detectable pressure by four orders of magnitude, surpassing the capabilities of previously reported self-adhesive sensors (Figure 4H),^{40,41} with a minimum detectable pressure comparable with state-of-the-art micro-electro-mechanical systems sensors used for measuring air pressure.³⁴

Application showcase of the underwater self-adhesive pressure sensors

To showcase the practical application of the self-adhesive underwater pressure sensor in underwater target recognition, we conducted an experimental setup to assess its effectiveness in detecting and categorizing various underwater targets, as illustrated in Figure 5A. A hybrid CNT-based pressure sensor was adhered to a machine ship to capture the target signals (Figure S21). Within a water tank, a speaker positioned at the tank base was computer controlled to generate signals with diverse frequencies and amplitudes, simulating different targets. Each target signal was collected by our sensor for 10 s at a sampling rate of 50. Thus, 500 data points per target signal were recorded. The data were wirelessly transmitted to a computer in real time and underwent preprocessing, feature extraction, and classification using an artificial neural network to achieve target recognition (Figure 5B).

We conducted simulations involving six distinct targets, each characterized by unique frequencies and signal strengths. Figure 5C portrays the recorded signals originating from these six distinct targets, accompanied by their respective frequency spectra, as illustrated in Figure 5D. These simulated signal sources were designed with pressure amplitudes of 18 mPa, aligned with their characteristic frequencies of 5, 7, 9, 4, 3, and 6 Hz, corresponding to targets 1 through 6, respectively. Deliberate measures were taken to establish low signal feature contrast, thereby emulating challenging scenarios involving objects or classes with similarities, as well as signals or features associated with weak targets.

We repeated the data collection process 20 times, generating a dataset of 120 samples. To visualize and analyze the collected data, we employed the t-distributed stochastic neighbor embedding technique for dimensionality reduction.⁴² The clustering results clearly demonstrate the grouping of signals with similar characteristics, facilitating clear differentiation between different targets based on their extracted features (Figure S22A). Leveraging a support vector machine neural network, we achieved an impressive average classification accuracy of 100%, as demonstrated by the confusion map in Figure S22B.

The pressure sensors utilizing aligned or nonaligned CNTs by themselves proved inadequate for achieving satisfactory target recognition in this particular endeavor, exhibiting average classification accuracies of 36% and 40%, respectively (Figures S22C–S22F). This result emphasizes the significance of sensor

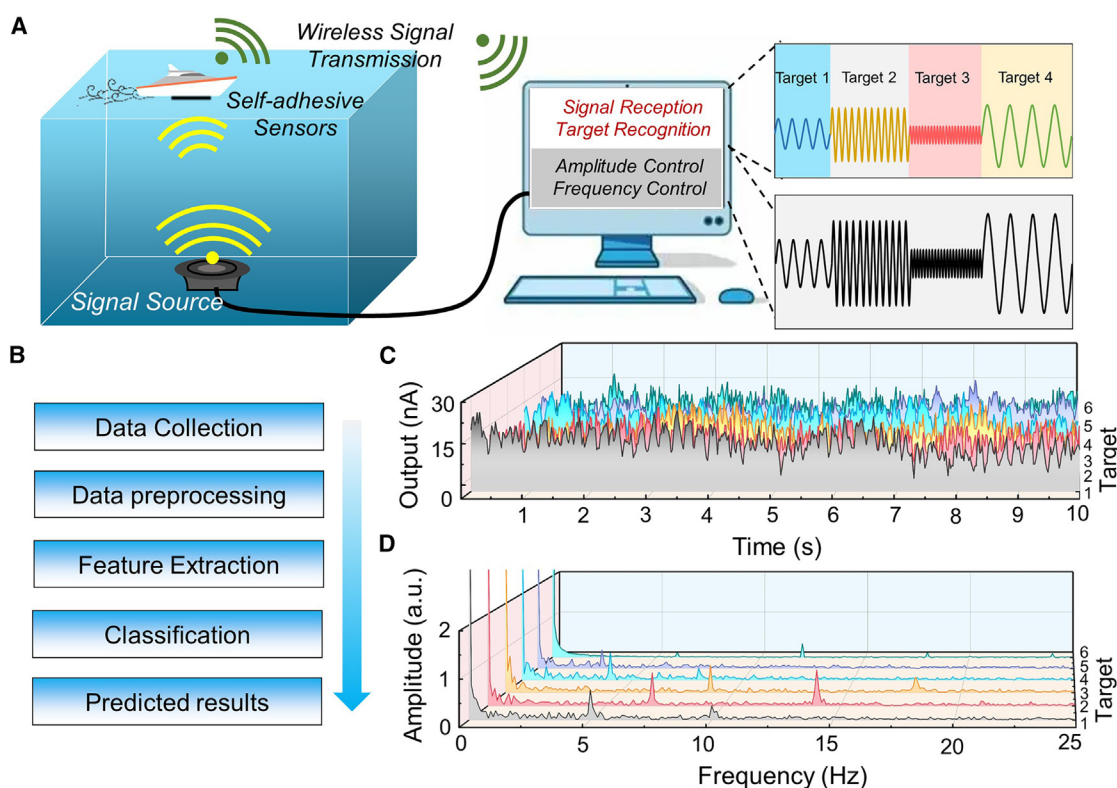


Figure 5. Application showcase of the self-adhesive underwater pressure sensors

(A) Demonstration of self-adhesive underwater pressure sensors in underwater target recognition and classification.

(B) Process of target recognition by machine learning.

(C) Six different simulated signals are used for the classification.

(D) Frequency spectra of six different simulate signals.

sensitivity and low detection limit in enabling precise and reliable target recognition. These factors determine the quality of input for the artificial neural network and its ability to extract target features, particularly under challenging conditions characterized by low-intensity signals.

In another test, we conducted field trials at Yujia Lake in Wuhan, China, as documented in [Video S2](#). During these trials, the sensor was affixed to an orange-colored boat, and real-time signal transmission to the shore was facilitated via remote control. A blue boat, configured with the control parameters outlined in [Figure S23](#), was maneuvered in close proximity to the orange boat, serving as the designated detection target. Given the inherently noisy surroundings near the lake, our primary mode of target detection relied upon the capacity of our sensor to discern water disturbances generated by the moving target during the test. Benefiting from the proficiency of the sensor in detecting even faint signals, we achieved successful long-range location monitoring of the blue boat. Although the sensor operates by harnessing the double electric layer effect on the surface of CNTs, which depends on the presence of ions from the water, we have demonstrated its functionality in Yujia Lake, which is a freshwater lake. There are enough electrolytes present in the lake, although there was some attenuation in the signal.² As demonstrated, for the precise identification of un-

derwater targets over extended distances, a transition from contact based to non-contact detection is imperative. In contrast to stationary, fixed-point detection, a mobile non-contact approach significantly minimizes disturbances to the marine ecosystem, mitigates the risk of harming delicate marine organisms or structures, and enables continuous, remote monitoring without direct interference.^{9,43,44}

Conclusion

In conclusion, we successfully developed a self-adhesive underwater pressure sensor utilizing a hybrid CNT assembly, enabling non-contact detection of underwater targets. The unique structural design of the hybrid CNT assembly effectively addresses the trade-off between sensing and adhesion functions, resulting in a secure fixation and a low detection limit as low as 18 mPa. Furthermore, the sensor exhibits a flat frequency response and vertical directionality due to its uniform and highly aligned structure. With a shear adhesion strength of 23.24 N/cm², it can withstand water pressure impacts up to 1.67 L/s and high-speed operation tests at 10 km/h, demonstrating robust performance and adaptability in complex underwater environments. By integrating the exceptional sensing properties with artificial neural networks, we have achieved mobile recognition of diverse simulated underwater targets. These breakthrough advancements in

sensor performance offer a highly promising solution for non-contact, long-distance target detection underwater.

In the pursuit of advanced underwater target monitoring, the challenge of differentiating between multiple targets at the same time has inspired the need for complex sensor arrays. Future developments in the field envision a holistic approach that integrates cutting-edge technologies to create an integrated sensor suite. In addition to our high-precision pressure detection sensors, this suite will include electromagnetic sensors for accurate detection of metallic targets, infrared sensors capable of capturing thermal signatures, and optical cameras to provide visual recognition. It is expected that the seamless integration of these different sensor modalities will create synergies that will enable real-time, multi-dimensional insights into the underwater environment. This advanced array of sensors will not only improve the ability to discriminate between different targets, but will also contribute to a deeper understanding of underwater ecosystems, facilitating a variety of applications ranging from marine research and environmental monitoring to security defense. As technology continues to evolve, the trajectory of underwater target monitoring will point to an era of comprehensive, intelligent and adaptable sensor systems.

EXPERIMENTAL PROCEDURES

Resource availability

Lead contact

Further information and requests for resources and reagents should be directed to and will be fulfilled by the lead contact, Ming Xu (ming.xu@hust.edu.cn).

Materials availability

This study did not generate new unique reagents.

Data and code availability

The project file of COMSOL simulation can be found in: <https://doi.org/10.5281/zenodo.10020263>. The target classification is achieved through MATLAB ANN toolbox. Other data needed to evaluate the conclusions in the paper are present in the paper and/or supplemental information. Additional data related to this paper can be requested from the lead contact.

Synthesis procedures

Synthesis of hybrid CNT assemblies

Hybrid CNT assemblies were synthesized through the water-assisted CVD process carried out at a temperature of 780°C. Ethylene (C₂H₄) was employed as the carbon source during this synthesis. Initially, a silicon (Si) wafer was prepared, onto which a 40-nm-thick Al₂O₃ buffer layer and a 3-nm Fe catalytic layer were subsequently deposited. The catalyst-coated substrates were then introduced into a 3-inch diameter quartz tube and subjected to heating at 780°C. Hydrogen and helium gases, acting as carrier gases, were utilized with a total flow rate of 1,000 sccm to facilitate the growth process. During this phase, the carbon source ethylene was thermally cracked at 780°C, allowing carbon atoms to infiltrate the iron atoms of the catalyst and precipitate, fostering CNT growth. The synthesis process occurred in two distinct stages. In the first stage, a 7-min growth period was dedicated to producing high-density oriented CNT arrays using a C₂H₄ flow rate of 120 sccm. Subsequently, in the second stage, a 3-min duration was allotted to cultivate low-density non-oriented CNT arrays with a C₂H₄ flow rate of 30 sccm. To enable CNT growth within the 20- to 40-min window at 780°C, C₂H₄ was introduced into the mixed gas of argon and nitrogen, while closely controlling the water vapor concentration at approximately 75 ppm.

Synthesis of aligned CNT arrays

For the synthesis of aligned CNT arrays, all steps remained the same as for the hybrid CNT assembly except for the growth step, which extended to 10 min under a C₂H₄ flow rate of 120 sccm.

Synthesis of nonaligned CNT assemblies

For the synthesis of the nonaligned CNT assemblies, the catalyst layer was subjected to a reactive ion etching technique with power of 50 W, time of 10 min prior to CVD growth. All other steps for the nonaligned CNT assembly were identical to those for the aligned CNT arrays.

Material characterizations

SEM (Nova NanoSEM 450, FEI) and TEM (Tecnai G2-20, FEI) were used for characterizing the microstructure of three CNT arrays. Compression stress-strain curves of CNT array were measured using a universal testing system (AGS-100NX, Shimadzu) and a crosshead speed of 3 mm min⁻¹. The purity of three CNT arrays (with respect to residual catalyst) were evaluated using a thermogravimetric analyzer (Q50, TA Instrument) and a heating rate of 10°C min⁻¹ in an atmosphere of oxygen. The Raman spectra were acquired by Raman microscope (LabRAM HR800) with an excitation wavelength of 532 nm. The mechanical properties of hybrid CNT assembly were evaluated using Dynamic mechanical analysis (AresG2-128, TA Instrument). The roughness of adhesion substrates was measured using an AFM (SPM-9700HT, Shimadzu).

Adhesion performance test

The adhesion performance of the self-adhesive underwater pressure sensor was evaluated using the setup depicted in Figure S10. The size of the sensor sample was 5 × 5 mm. After adhering the self-adhesive pressure sensor to the substrate in air, it was immersed in a simulated marine environment (0.6 mol/L NaCl). The universal testing system was used to record the force-displacement curve during the detachment process, and the work of detachment was obtained by integrating the force-displacement curve.

Sensing performance test

The sensing performance of the self-adhesive underwater pressure sensor was conducted using the setup shown in Figure S14. The working electrode was adhered to a 5 × 5 mm copper substrate and placed in an underwater environment and subjected to pressure applied by a Tomlinson Holman Experiment (THX)-certified waterproof speaker. The speaker was positioned 3 cm away from the self-adhesive pressure sensor, and the magnitude and frequency of the pressure applied by the speaker were controlled using computer software. The signal acquisition of the self-adhesive underwater pressure sensor was measured using a CH Instruments electrochemical workstation (model 760E). The ±3 dB bandwidth criterion was employed to evaluate frequency response characteristics of the sensors, ensuring that the minimum value did not fall below 0.727 times the maximum value. As a result, the fluctuation range did not exceed 27.3%. The self-adhesive underwater pressure sensor conformed to the standard frequency response characteristics within a pressure range of 18–178 mPa and a frequency range of 1–10 Hz. For deep-sea simulation testing, diverse water depths are emulated by exerting pre-pressure on the sensor through a hydrostatic motor in a water tank. An electric scale is positioned beneath the sensor to measure the precise pre-pressure value. The simulated water pressure (P) can be calculated using the formula P = F/A, where F represents the pre-pressure and A is the area of the sensor. Considering a water pressure conversion rate of approximately 10 kPa/m of water depth, we applied pre-pressures of 0, 200, 400, and 600 kPa to represent water depths of 0, 20, 40, and 60 m, respectively.

SUPPLEMENTAL INFORMATION

Supplemental information can be found online at <https://doi.org/10.1016/j.device.2023.100223>.

ACKNOWLEDGMENTS

The authors acknowledge financial support from the National Key R&D Program of China (grant no. 2022YFB3807700), the Natural Science Foundation of Hubei Province, China (grant no. 2022CFA031), the National Natural Science Foundation of China (grant no. 51972127), and the Science, Technology and Innovation Commission of Shenzhen Municipality (grant nos. JCYJ20190809102607400).

and JCYJ20210324135207020). The authors appreciate Prof. Yuelong Liu and Prof. Shaobo Qu (School of Physics, Huazhong University of Science and Technology) for their help and support in numerical simulation. The authors also appreciate Mr. Pan Li (Engineer in the Optoelectronic Micro & Nano Fabrication and Characterizing Facility, Wuhan National Laboratory for Optoelectronics of Huazhong University of Science and Technology) for support in material fabrication (reactive ion etching).

AUTHOR CONTRIBUTIONS

M.X. generated the concept, supervised the study, and edited the paper. S.Y. supervised the sensor test at Yujia Lake. H.L. wrote the manuscript, performed the sensing performance test, demonstration, and numerical simulation. Y.L. and H.L. performed the sensor test at Yujia Lake. Z.Y. performed the adhesion performance test. H.L. and Q.Z. developed the synthesis technique of hybrid CNT assemblies.

DECLARATION OF INTERESTS

The authors declare no competing interests.

INCLUSION AND DIVERSITY

We support inclusive, diverse, and equitable conduct of research.

Received: August 3, 2023

Revised: August 30, 2023

Accepted: December 6, 2023

Published: January 2, 2024

REFERENCES

- Zou, Y., Tan, P., Shi, B., Ouyang, H., Jiang, D., Liu, Z., Li, H., Yu, M., Wang, C., Qu, X., et al. (2019). A bionic stretchable nanogenerator for underwater sensing and energy harvesting. *Nat. Commun.* **10**, 2695.
- Zhang, M., Fang, S., Nie, J., Fei, P., Aliev, A.E., Baughman, R.H., and Xu, M. (2020). Self-Powered, Electrochemical Carbon Nanotube Pressure Sensors for Wave Monitoring. *Adv. Funct. Mater.* **30**, 2004564.
- Thorp, W.H. (1965). Deep-Ocean Sound Attenuation in the Sub- and Low-Kilocycle-per-Second Region. *J. Acoust. Soc. Am.* **38**, 648–654.
- Francois, R.E., and Garrison, G.R. (1982). Sound absorption based on ocean measurements: Part I: Pure water and magnesium sulfate contributions. *J. Acoust. Soc. Am.* **72**, 896–907.
- Francois, R.E., and Garrison, G.R. (1982). Sound absorption based on ocean measurements. Part II: Boric acid contribution and equation for total absorption. *J. Acoust. Soc. Am.* **72**, 1879–1890.
- Zhang, J., Xiang, X., and Li, W. (2023). Advances in Marine Intelligent Electromagnetic Detection System, Technology, and Applications: A Review. *IEEE Sensor. J.* **23**, 4312–4326.
- Yin, J., Men, W., Han, X., and Guo, L. (2020). Integrated waveform for continuous active sonar detection and communication. *IET Radar, Sonar Navig.* **14**, 1382–1390.
- Xu, Y., Zhao, S., Shang, W., Jia, P., Gao, J., Korochentsev, V., and Grischenko, V. (2022). Active Electric Anomaly Detection Method for Underwater Targets Based on the Orthonormal Basis Function. *J. Mar. Sci. Eng.* **10**, 407.
- Ma, L., Gulliver, T.A., Zhao, A., Ge, C., and Bi, X. (2019). Underwater broadband source detection using an Acoustic Vector Sensor with an adaptive passive matched filter. *Appl. Acoust.* **148**, 162–174.
- Rayment, W., Webster, T., Brough, T., Jowett, T., and Dawson, S. (2017). Seen or heard? A comparison of visual and acoustic autonomous monitoring methods for investigating temporal variation in occurrence of southern right whales. *Mar. Biol.* **165**, 12.
- Kavet, R., Wyman, M.T., and Klimley, A.P. (2016). Modeling magnetic fields from a DC power cable buried beneath San Francisco bay based on empirical measurements. *PLoS One* **11**, e0148543.
- Page, B.R., Lambert, R., Mahmoudian, N., Newby, D.H., Foley, E.L., and Kornack, T.W. (2021). Compact Quantum Magnetometer System on an Agile Underwater Glider. *Sensors* **21**, 1092.
- Yu, Z., Xiao, C., and Zhou, G. (2014). Multi-Objectivization-Based Localization of Underwater Sensors Using Magnetometers. *IEEE Sensor. J.* **14**, 1099–1106.
- Liu, J., Li, B., Guan, W., Gong, S., Liu, J., and Cui, J. (2020). A Scale-Adaptive Matching Algorithm for Underwater Acoustic and Optical Images. *Sensors* **20**, 4226.
- Liu, T., Wang, N., Zhang, L., Ai, S., and Du, H. (2020). A Novel Visual Measurement Method for Three-Dimensional Trajectory of Underwater Moving Objects Based on Deep Learning. *IEEE Access* **8**, 186376–186392.
- Wu, S., Li, H., Futaba, D.N., Chen, G., Chen, C., Zhou, K., Zhang, Q., Li, M., Ye, Z., and Xu, M. (2022). Structural Design and Fabrication of Multifunctional Nanocarbon Materials for Extreme Environmental Applications. *Adv. Mater.* **34**, 2201046.
- Wang, Z., Zhou, H., Liu, D., Chen, X., Wang, D., Dai, S., Chen, F., and Xu, B.B. (2022). A Structural Gel Composite Enabled Robust Underwater Mechanosensing Strategy with High Sensitivity. *Adv. Funct. Mater.* **32**, 2201396.
- Liu, X., Zhang, Q., and Gao, G. (2020). Solvent-Resistant and Nonswellable Hydrogel Conductor toward Mechanical Perception in Diverse Liquid Media. *ACS Nano* **14**, 13709–13717.
- Liu, Q., Liu, Y., Shi, J., Liu, Z., Wang, Q., and Guo, C.F. (2021). High-Porosity Foam-Based Iontronic Pressure Sensor with Superhigh Sensitivity of 9280 kPa⁻¹. *Nano-Micro Lett.* **14**, 21.
- Wang, Q., Xiao, P., Zhou, W., Liang, Y., Yin, G., Yang, Q., Kuo, S.-W., and Chen, T. (2022). Bioinspired Adaptive, Elastic, and Conductive Graphene Structured Thin-Films Achieving High-Efficiency Underwater Detection and Vibration Perception. *Nano-Micro Lett.* **14**, 62.
- Cheng, Y., Guo, C., Li, S., Deng, K., Tang, J., Luo, Q., Zhang, S., Chang, Y., and Pan, T. (2022). Aquatic Skin Enabled by Multi-Modality Iontronic Sensing. *Adv. Funct. Mater.* **32**, 2205947.
- Hata, K., Futaba, D.N., Mizuno, K., Namai, T., Yumura, M., and Iijima, S. (2004). Water-Assisted Highly Efficient Synthesis of Impurity-Free Single-Walled Carbon Nanotubes. *Science* **306**, 1362–1364.
- Xu, M., Futaba, D.N., Yumura, M., and Hata, K. (2012). Alignment Control of Carbon Nanotube Forest from Random to Nearly Perfectly Aligned by Utilizing the Crowding Effect. *ACS Nano* **6**, 5837–5844.
- Xu, M., Futaba, D.N., Yamada, T., Yumura, M., and Hata, K. (2010). Carbon Nanotubes with Temperature-Invariant Viscoelasticity from -196°C to 1000°C. *Science* **330**, 1364–1368.
- Qu, L., Dai, L., Stone, M., Xia, Z., and Wang, Z.L. (2008). Carbon Nanotube Arrays with Strong Shear Binding-On and Easy Normal Lifting-Off. *Science* **322**, 238–242.
- Lu, D., Yan, Y., Deng, Y., Yang, Q., Zhao, J., Seo, M.-H., Bai, W., MacEwan, M.R., Huang, Y., Ray, W.Z., and Rogers, J.A. (2020). Bioresorbable Wireless Sensors as Temporary Implants for In Vivo Measurements of Pressure. *Adv. Funct. Mater.* **30**, 2003754.
- Herbert, R., Lim, H.-R., Rigo, B., and Yeo, W.-H. (2022). Fully implantable wireless batteryless vascular electronics with printed soft sensors for multiplex sensing of hemodynamics. *Sci. Adv.* **8**, eabm1175.
- Boutry, C.M., Kaizawa, Y., Schroeder, B.C., Chortos, A., Legrand, A., Wang, Z., Chang, J., Fox, P., and Bao, Z. (2018). A stretchable and biodegradable strain and pressure sensor for orthopaedic application. *Nat. Electron.* **1**, 314–321.
- Shin, J., Yan, Y., Bai, W., Xue, Y., Gamble, P., Tian, L., Kandela, I., Haney, C.R., Spees, W., Lee, Y., et al. (2019). Bioresorbable pressure sensors protected with thermally grown silicon dioxide for the monitoring of chronic diseases and healing processes. *Nat. Biomed. Eng.* **3**, 37–46.

30. Shi, L., Li, Z., Chen, M., Qin, Y., Jiang, Y., and Wu, L. (2020). Quantum effect-based flexible and transparent pressure sensors with ultrahigh sensitivity and sensing density. *Nat. Commun.* 11, 3529.
31. Ma, L., Wang, J., He, J., Yao, Y., Zhu, X., Peng, L., Yang, J., Liu, X., and Qu, M. (2021). Ultra-sensitive, durable and stretchable ionic skins with biomimetic micronanostructures for multi-signal detection, high-precision motion monitoring, and underwater sensing. *J. Mater. Chem. A Mater.* 9, 26949–26962.
32. Kim, D., and Yoon, J. (2020). Water-Borne Fabrication of Stretchable and Durable Microfibers for High-Performance Underwater Strain Sensors. *ACS Appl. Mater. Interfaces* 12, 20965–20972.
33. Zhang, J., Yao, H., Mo, J., Chen, S., Xie, Y., Ma, S., Chen, R., Luo, T., Ling, W., Qin, L., et al. (2022). Finger-inspired rigid-soft hybrid tactile sensor with superior sensitivity at high frequency. *Nat. Commun.* 13, 5076.
34. Goel, N., Costanzo, F., and Tadigadapa, S. (2019). Experimental Studies in Micromachined AT-Cut Quartz-Based Differential Vacuum Gauges. *IEEE Sensor. J.* 19, 2047–2054.
35. Nassar, J.M., Khan, S.M., Velling, S.J., Diaz-Gaxiola, A., Shaikh, S.F., Geraldi, N.R., Torres Sevilla, G.A., Duarte, C.M., and Hussain, M.M. (2018). Compliant lightweight non-invasive standalone “Marine Skin” tagging system. *npj Flex. Electron.* 2, 13.
36. Ramanathan, A.K., Headings, L.M., and Dapino, M.J. (2021). Differential pressure sensor using flexible piezoelectrics with pyroelectric compensation. *Smart Mater. Struct.* 30, 035020.
37. Wang, L., Zhao, Y., Yang, Y., Pang, X., Hao, L., and Zhao, Y. (2022). Piezoresistive 4H-SiC Pressure Sensor With Diaphragm Realized by Femtosecond Laser. *IEEE Sensor. J.* 22, 11535–11542.
38. Zhou, X., Zhang, R., Li, L., Zhang, L., Liu, B., Deng, Z., Wang, L., and Gui, L. (2019). A liquid metal based capacitive soft pressure microsensor. *Lab Chip* 19, 807–814.
39. Yu, Z., and Wu, P. (2021). Underwater Communication and Optical Camouflage Ionogels. *Adv. Mater.* 33, 2008479.
40. Chun, S., Kim, D.W., Kim, J., and Pang, C. (2019). A transparent, glue-free, skin-attachable graphene pressure sensor with micropillars for skin-elasticity measurement. *Nanotechnology* 30, 335501.
41. Pang, C., Koo, J.H., Nguyen, A., Caves, J.M., Kim, M.-G., Chortos, A., Kim, K., Wang, P.J., Tok, J.B.-H., and Bao, Z. (2015). Highly Skin-Conformal Microhairy Sensor for Pulse Signal Amplification. *Adv. Mater.* 27, 634–640.
42. van der Maaten, L., and Hinton, G. (2008). Visualizing Data using t-SNE. *J. Mach. Learn. Res.* 9, 2579–2605. <https://www.jmlr.org/papers/v9/vandermaaten08a.html>.
43. Wang, M., Qiu, B., Zhu, Z., Ma, L., and Zhou, C. (2022). Passive tracking of underwater acoustic targets based on multi-beam LOFAR and deep learning. *PLoS One* 17, e0273898.
44. Hu, G., Wang, K., and Liu, L. (2021). Underwater Acoustic Target Recognition Based on Depthwise Separable Convolution Neural Networks. *Sensors* 21, 1429.